Journal of Alloys and Compounds 623 (2015) 109–116

Contents lists available at ScienceDirect

Journal of Alloys and Compounds

journal homepage: www.elsevier.com/locate/jalcom

Thermodynamic destabilisation of MgH_2 and $NaMgH_3$ using Group IV elements Si, Ge or Sn

Anna-Lisa Chaudhary [a,b,*], Mark Paskevicius [a], Drew A. Sheppard [a], Craig E. Buckley [a]

[a] Department of Imaging and Applied Physics, Fuel and Energy Technology Institute, Curtin University, Australia
[b] Institute of Materials Research, Materials Technology, Helmholtz-Zentrum Geesthacht, Max-Planck-Strasse 1, D-21502 Geesthacht, Schleswig-Holstein, Germany

ARTICLE INFO

Article history:
Received 29 August 2014
Received in revised form 7 October 2014
Accepted 15 October 2014
Available online 23 October 2014

Keywords:
Magnesium hydride
Sodium magnesium hydride
Desorption
Destabilisation
Reaction kinetics
Thermodynamics

ABSTRACT

The addition of Group IV elements of Si, Ge or Sn to Mg-based hydrides has led to the successful destabilisation of MgH_2 or $NaMgH_3$, resulting in hydrogen release at lower temperatures. This is the first time a direct comparison has been made with all the samples prepared and characterised using identical conditions. Pure MgH_2 desorbs hydrogen at a pressure of 1 bar at 282 °C, a temperature too high for typical mobile applications. The addition of Group IV metals to MgH_2 causes the formation of intermetallic compounds (Mg_2Si, Mg_2Ge and Mg_2Sn) upon hydrogen release. Theoretical calculations show promising thermodynamic equilibrium conditions for these systems. Experimentally, these conditions were difficult to achieve, however, hydrogen desorption results show that Ge has the most significant effect in allowing low temperature hydrogen release, followed by Sn, then Si. It was found that Si also has a beneficial effect on $NaMgH_3$, reducing the desorption temperature.

1. Introduction

Hydrogen based energy systems have the capacity to store clean, sustainable energy now and for future generations. As global energy demands rise, so do concerns over climate change and depleting fossil fuel resources [1], the shift towards energy production from renewable resources has gained considerable momentum [2,3], Hydrogen storage systems can be combined with fuel cells for on demand electricity or for use in mobile transport to address these environmental energy issues [4,5]. Finding an efficient and safe way to store hydrogen is one of the challenges to hydrogen fuel usage [6,7].

The most promising option being explored is the solid-state storage of hydrogen in metal hydrides [8–10]. Magnesium is an attractive choice as it is inexpensive, abundant and has a high hydrogen storage capacity of 7.7 wt.% hydrogen in the form of MgH_2 (Reaction (1)) [11–13]. The drawbacks, however, include slow reaction kinetics and the strong binding energy between magnesium and hydrogen [14]. The kinetic issues in the Mg–H system have largely been overcome with a range of additives introduced via ball milling, that provide particle size refinement and enable rapid reaction kinetics [15]. However, the high thermodynamic stability of MgH_2 is more difficult to overcome, where the thermodynamics are known to be: $\Delta H = 74$ kJ/mol H_2 and $\Delta S = 133.4$ J/mol H_2/K [16]. At thermodynamic equilibrium these thermodynamic properties equate to a 1 bar H_2 desorption temperature of 282 °C, too high for typical mobile applications.

$$\mathbf{MgH_2} \rightarrow \mathbf{Mg} + \mathbf{H_2(g)} \quad (1)$$

$NaMgH_3$ is another viable hydrogen storage compound with a storage capacity of 6 wt.% H_2. $NaMgH_3$ undergoes a two-step desorption process that releases *ca.* 4 wt.% and 2 wt.% of hydrogen gas in each step [17,18]. The first step (Reaction (2)) is the most relevant to practical applications because of its lower operating temperature and the benefit of restricting molten Na metal formation. Similar to MgH_2, $NaMgH_3$ also contains strongly bound hydrogen [19] resulting in high thermodynamic stability. A recent study measured the thermodynamic properties of the first decomposition step of $NaMgH_3$ as $\Delta H = 86.6$ kJ/mol H_2 and $\Delta S = 132.2$ J/mol H_2/K, giving an operational temperature of 382 °C at 1 bar H_2 [20].

$$\mathbf{NaMgH_3} \rightarrow \mathbf{Mg} + \mathbf{NaH} + \mathbf{H_2(g)} \quad (2)$$

Thermodynamic destabilisation of both MgH_2 and $NaMgH_3$ can be achieved by introducing another reactive element to allow for the formation of a more energetically favourable intermetallic upon hydrogen desorption. Si is a well-known additive that has been used to destabilize MgH_2 [21–24] (Reaction (3)), significantly reducing the enthalpy of reaction to 38.9 kJ mol H_2^{-1} [24]. This reduction in

* Corresponding author at: Institute of Materials Research, Materials Technology, Helmholz Zentrum Geesthacht, Germany. Tel.: +49 (0) 4152872647.
E-mail address: anna-lisa.chaudhary@hzg.de (A.-L. Chaudhary).

http://dx.doi.org/10.1016/j.jallcom.2014.10.086
0925-8388/

enthalpy results in a theoretical desorption temperature of 25 °C at 1 bar with a H_2 capacity of 5 wt.% [24]. Attempts to achieve thermodynamic equilibrium of the Mg–Si–H system experimentally have been limited by reaction kinetics [22,25]. The destabilisation of $NaMgH_3$ has also been achieved with the addition of Si to the system (Reaction (4)), with the desorption temperature of pure $NaMgH_3$ being reduced from 350 to 250 °C [19]. The theoretical hydrogen capacity of $NaMgH_3$ is also reduced from 4 wt.% to 3.13 wt.% once Si is added.

After Si, the next Group IV elements are Ge and Sn, which also form intermetallics with Mg [26–28]. Ge has similar properties to Si and has also been studied as a destabilising additive to MgH_2 [29] (Reaction (5)). Adding Ge to the system results in a reduced theoretical storage capacity of 3.22 wt.% H_2. Walker et al. [29] found that the enthalpy of desorption with the addition of Ge was reduced by 60 kJ mol^{-1} H_2 to a value of ΔH = 14 kJ mol^{-1} H_2. The Mg–Ge–H system is investigated further herein by directly comparing changes in dehydrogenation properties with its sister Si system.

Sn can also be added to MgH_2 (Reaction (6)) and the increase in molecular mass with the stoichiometric addition of Sn reduces the hydrogen storage capacity to 2.36 wt.% H_2. Experimentally, the addition of Sn to MgH_2 has already proven to be an effective destabilising element for MgH_2 [30–32] however, there has been no direct comparison made between Si, Ge and Sn with consistent preparation and characterisation techniques. Therefore, this study aims to destabilise hydrogen desorption from MgH_2 using these Group IV elements with the same mixing process and desorption experimentation. Destabilisation of $NaMgH_3$ will also be investigated by the same processes by adding Si.

$$\mathbf{2MgH_2 + Si \leftrightarrow Mg_2Si + 2H_2(g)} \quad (3)$$

$$\mathbf{2NaMgH_3 + Si \rightarrow Mg_2Si + 2NaH + 2H_2(g)} \quad (4)$$

$$\mathbf{2MgH_2 + Ge \leftrightarrow Mg_2Ge + 2H_2(g)} \quad (5)$$

$$\mathbf{2MgH_2 + Sn \leftrightarrow Mg_2Sn + 2H_2(g)} \quad (6)$$

2. Experimental

All material handling was undertaken in an argon atmosphere glovebox (UnilabGlovebox, mBraun, Germany). An automatic gas purifier unit controlled the oxygen and moisture levels to limit any risk of contamination (O_2 < 1 ppm, H_2O < 1 ppm). Magnesium hydride (H_2 storage grade, 95%), silicon powder (−325 mesh, 99%), germanium (>99.999%) and tin (>99%) were supplied by Sigma–Aldrich. $NaMgH_3$ synthesis is described in a previous publication [20].

For direct comparison with MgH_2, theoretical equilibrium pressures of MgH_2 mixed with Si, Ge and Sn were calculated using thermodynamic data for MgH_2 from Bogdanović et al. [33]and thermodynamic data for the other compounds from the software program HSC (HSC Chemistry 6.12 software, Outotech Research). This software allows the user to enter in known values (from literature) for enthalpy and entropy and calculate theoretical thermodynamic properties over a specified temperature range and pressure.

Table 1
Pure MgH_2 and Si addition to MgH_2 crystallite size from Rietveld refinement.

Sample	Phase	Structure	wt.%	Cryst. size (nm)
MgH_2	β-MgH_2	Tetragonal, 136, *P42/mnm*	96.3	86 ± 1
R_{wp} = 8.1% (as supplied)	Mg	Hexagonal, 194, *P63/mmc*	3.7	93 ± 12
Si R_{wp} = 7% (as supplied)	Si	Cubic, 227, *Fd-3m*	100	211 ± 3
$2MgH_2$ + Si	β-MgH_2	Tetragonal, 136, *P42/mnm*	45.2	7.6 ± 0.1
R_{wp} = 4.8% (cryomilled)	γ-MgH_2	Orthorhombic, 60, *Pbcn*	21.6	2.4 ± 0.2
	Mg	Hexagonal, 194, *P63/mmc*	1.0	58 ± 13
	Si	Cubic, 227, *Fd-3m*	32.2	67 ± 1
Mg_2Si	Mg_2Si	Cubic, 225, *Fm-3m*	97.1	62 ± 1
R_{wp} = 7.9% (desorbed)	Si	Cubic, 227, *Fd-3m*	2.4	100 ± 13
	MgO	Cubic, 225, *Fm-3m*	0.5	2.3 ± 0.1

Table 2
Ge addition to MgH_2, crystallite size from Rietveld refinement.

Sample	Phase	Structure	wt.%	Cryst. size (nm)
Ge	Ge	Cubic, 227, *Fd-3m*	97.4	227 ± 4
R_{wp} = 8.7% (as supplied)	GeO_2	Trigonal, 152, *P3121*	2.6	58 ± 8
$2MgH_2$ + Ge	β-MgH_2	Tetragonal, 136, *P42/mnm*	38.1	5.6 ± 0.2
R_{wp} = 9% (cryomilled)	Ge	Cubic, 227, *Fd-3m*	61.9	35 ± 1
Mg_2Ge	Mg_2Ge	Cubic, 225, *Fm-3m*	95.9	73 ± 1
R_{wp} = 6.7% (desorbed)	Ge	Cubic, 227, *Fd-3m*	4.1	78 ± 3

Table 3
Sn addition to MgH_2, crystallite size from Rietveld refinement.

Sample	Phase	Structure	wt.%	Cryst. size (nm)
Sn R_{wp} = 8.1% (as supplied)	Sn	Tetragonal, 141, *I41/amd*	100	547 ± 16
$2MgH_2$ + Sn	β-MgH2	Tetragonal, 136, *P42/mnm*	26.4	7.0 ± 0.6
R_{wp} = 6.2% (cryomilled)	Sn	Tetragonal, 141, *I41/amd*	73.6	85 ± 3
Mg_2Sn	Mg_2Sn	Cubic, 225, *Fm-3m*	93.6	147 ± 5
R_{wp} = 7.8% (desorbed)	Sn	Tetragonal, 141, *I41/amd*	6.4	94 ± 7

The hydrides were mixed in stoichiometric ratios from Reactions (3)–(6), with Si, Ge or Sn in a SpexSamplePrep 6850 Freezer Mill (USA) at liquid nitrogen temperatures (77 K). The powders and stainless steel rod impactor were placed into a 14.3 cm^3 milling vial constructed from stainless steel and sealed with stainless steel end caps. The mill was programmed for a total grinding time of 30 min with a 2 min cooling interval for each minute of grinding.

X-ray diffraction (XRD) measurements were conducted using a D8 Advance (Bruker, Germany) X-ray diffractometer with a copper anode tube (λ = 1.5418 Å) and LynxEye detector. Scans were taken at a 2θ range of 10–100° with a 0.02° step size and 0.7 s exposure times per step. While in the glovebox, the sample was sealed within an airtight XRD holder made from a poly(methyl methacrylate), or PMMA, dome to prevent exposure to air and moisture during the measurements. Bruker *Diffracplus EVA* version 16 and *Diffracplus TOPAS* version 4.2 were used to identify crystalline compounds present and for Rietveld refinement respectively. An instrumental parameter file was used to eliminate instrumental line broadening for all analyses. Crystallite size values were taken from the LVol-IB (volume weighted mean column height) that incorporates Lorentzian and Gaussian convolutions varying in 2θ as a function of $\cos(\theta)^{-1}$ and $\tan(\theta)$ respectively. This method provides a volume weighted average crystallite size. Uncertainties were reported from *TOPAS* (bootstrap method of error determination). It should be noted that the grey plots at the bottom of each XRD figure (Figs. 2–5) are an indication of the difference between the raw data collected on the XRD equipment and Rietveld refinement. The R_{wp} values (Tables 1–4), or weighted profile *R*-factor value, also gives an indication of the accuracy of the simulated model. This discrepancy index uses an algorithm to optimize the model function so that a minimum of the weighted sum of squares differences between the experimental and computed intensities is calculated [34]. As a general rule, R_{wp} values 5% or less indicates an acceptable goodness of fit [34], however, this value largely depends on an over estimation of uncertainties and should only be used as a guide [34].

Scanning electron microscopy (SEM) of the materials was performed using a Zeiss Neon 40EsB (Zeiss, Germany). Specimens were prepared by distributing a small amount of powder onto carbon tape then coating with a 2–4 nm layer of high atomic elements, either gold or platinum, to produce a conductive layer and reduce charging of the sample during its interaction with the electrons in the SEM. All samples were exposed to air for a short period of time when transferred from the coating instrument as well as loading into the SEM chamber.

Table 4
Si addition to $NaMgH_3$, crystallite size from Rietveld Refinement.

Sample	Phase	Structure	wt.%	Crystallite size (nm)
$NaMgH_3$	$NaMgH_3$	Orthorhombic, 62, *Pnma*	76.3	31 ± 1
R_{wp} = 9.3% (synthesised from MgH_2 + NaH)	NaH	Cubic, 225, *Fm-3m*	2.2	7.7 ± 1.4
	MgH_2	Tetragonal, 136, *P42/mnm*	3.7	2.5 ± 0.7
	MgO	Cubic, 225, *Fm-3m*	17.8	1.3 ± 0.1
$2NaMgH_3$ + Si	$NaMgH_3$	Orthorhombic, 62, *Pnma*	60.9	10.7 ± 0.1
R_{wp} = 4.5% (cryomilled)	Si	Cubic, 227, *Fd-3m*	21.4	81 ± 1
	MgO	Cubic, 225, *Fm-3m*	17.7	1.4 ± 0.1
Mg_2Si, NaH	Mg_2Si	Cubic, 225, *Fm-3m*	47.7	44 ± 1
R_{wp} = 6.2% (desorbed)	NaH	Cubic, 227, *Fd-3m*	27.4	40 ± 1
	Si	Cubic, 227, *Fd-3m*	7.7	76 ± 3
	MgO	Cubic, 225, *Fm-3m*	17.2	2.2 ± 0.1

Hydrogen desorption properties were analysed using a manometric Sieverts apparatus where the sample cell was placed in a furnace and isothermal measurements taken over time (see [16] for more details). Each sample was held for 24 h at 50 °C and then at 50 °C increments through to a maximum temperature of 350 °C. If there was no hydrogen desorption detected after 2 h at 350 °C, the run was stopped.

Temperature programmed desorption (TPD) was also undertaken using a Stanford Research Systems Residual Gas Analyzer (RGA) 300 under vacuum. This method uses a turbo vacuum pump to achieve a low pressure atmosphere (10^{-5} - mbar) and identifies gases released from the system according to the atomic mass unit (amu) of the gas by a mass spectrometer. 20–30 mg of each sample was loaded into a sample cell and the system was outgassed at room temperature until all traces of argon were undetectable. An N-type thermocouple was attached to the outside the cell within proximity of the sample being analysed. The samples were heated from room temperature up to 600 °C at a rate of 2 °C min^{-1}.

3. Results and discussion

Theoretical comparisons between all compounds discussed in this article can be found in Fig. 1. Since $NaMgH_3$ enthalpy data

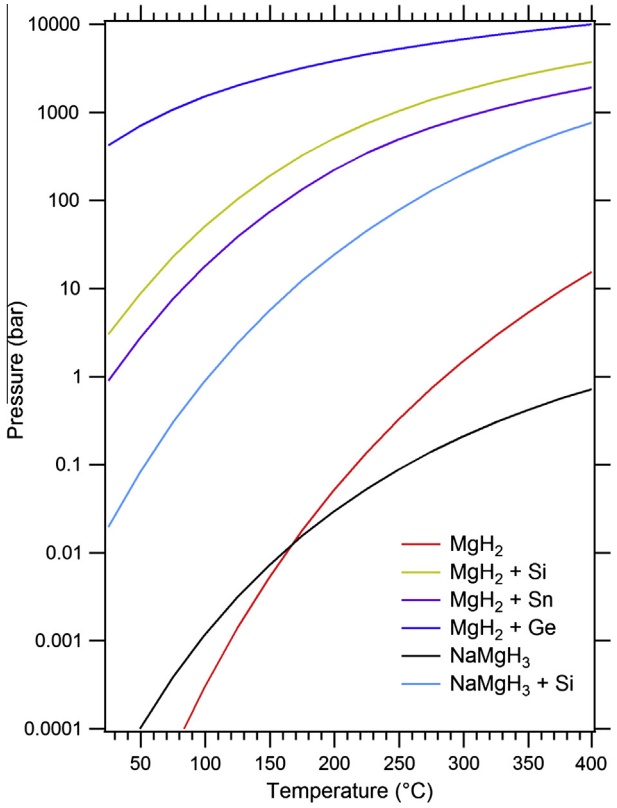

Fig. 1. Calculated equilibrium pressures for MgH_2 and $NaMgH_3$ with and without added Group IV elements.

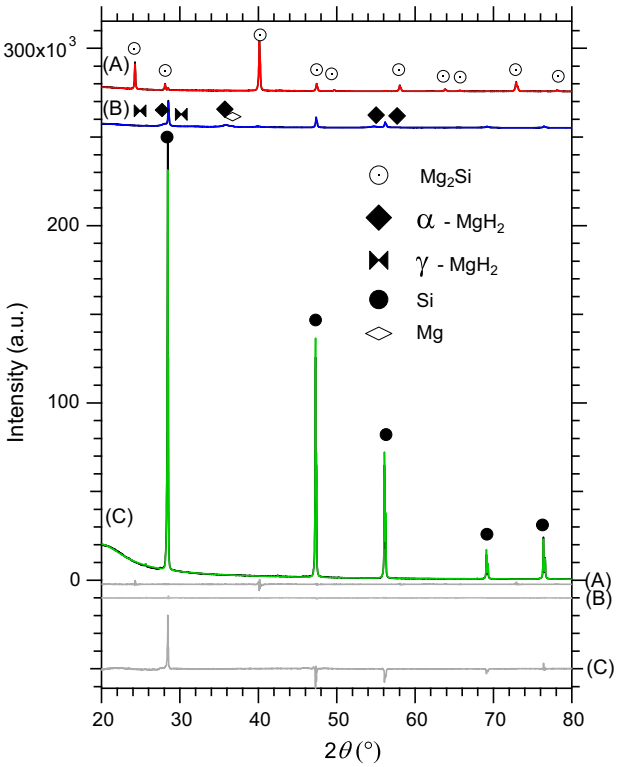

Fig. 2. XRD patterns of Si based experiments (A) MgH_2 and Si desorbed to form Mg_2Si, 24 h in 50–350 °C increments (B) Cryomilled with MgH_2 for 30 min (C) Si as supplied from Sigma–Aldrich.

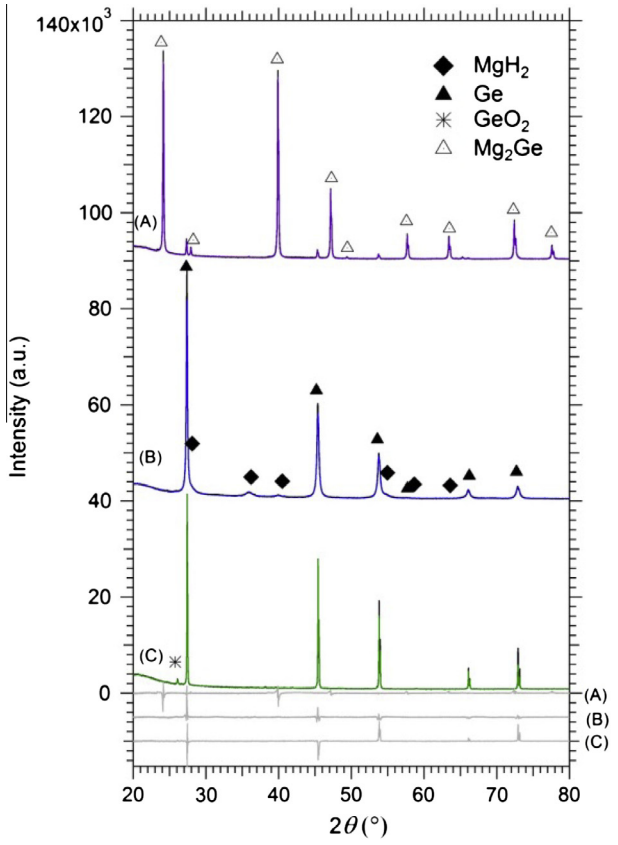

Fig. 3. XRD patterns of Ge based experiments (A) MgH_2 and Ge desorbed to form Mg_2Ge, 24 h in 50–350 °C increments (B) Cryomilled with MgH_2 for 30 min (C) Ge as supplied from Sigma–Aldrich.

was not available, the formation enthalpy and entropy were determined at 419 °C based on the values for NaH, Mg and H_2 at that temperature combined with enthalpy of hydrogen desorption, 86.6 kJ/mol H_2 (from $NaMgH_3$ via the reaction of $NaMgH_3$ - ↔ NaH + Mg + H_2 [20]). The heat capacity of $NaMgH_3$ is not experimentally known but was approximated as the sum of the heat capacities of its individual components: NaH and MgH_2. The veracity of this approached was confirmed with the isostructural phase, $NaMgF_3$. There is a difference of less than 3.5% between the heat capacity of $NaMgF_3$ [35] and the sum of the heat capacities for NaF and MgF_2 over the temperature range of 40–400 °C. The resulting standard enthalpy, ΔH_f, and entropy, ΔS_f, of formation at 25 °C are −143.0 kJ/mol and −208.0 J/mol K, respectively. The ΔH_f value is in good agreement with the value calculated by Bouhadda [36], −151.8 kJ/mol, using Density Functional Theory.

The results show that when mixed with either Si or Sn at temperatures less than 50 °C, hydrogen equilibrium pressure of less than 10 bar are achievable. However, at room temperature, MgH_2 combined with Ge, results in a hydrogen equilibrium pressure above 500 bar. These predictions indicate an improvement in the thermodynamic behaviour of hydrogen release when MgH_2 is combined with Si, Ge or Sn.

The comparison between $NaMgH_3$/Si with MgH_2/Si shows that the equilibrium pressure for the former is much lower than the latter at higher temperatures (Fig. 1). This indicates that reaction kinetics could be improved with an increase in temperature without thermodynamic restrictions (high pressures) coming into effect. This change in the reaction pathway would also lead to better hydrogen reabsorption into Mg_2Si. These results indicate that the addition of Group IV elements to MgH_2 or $NaMgH_3$ can lead to thermodynamically favourable desorption temperatures, thus creating a more practical hydrogen storage system.

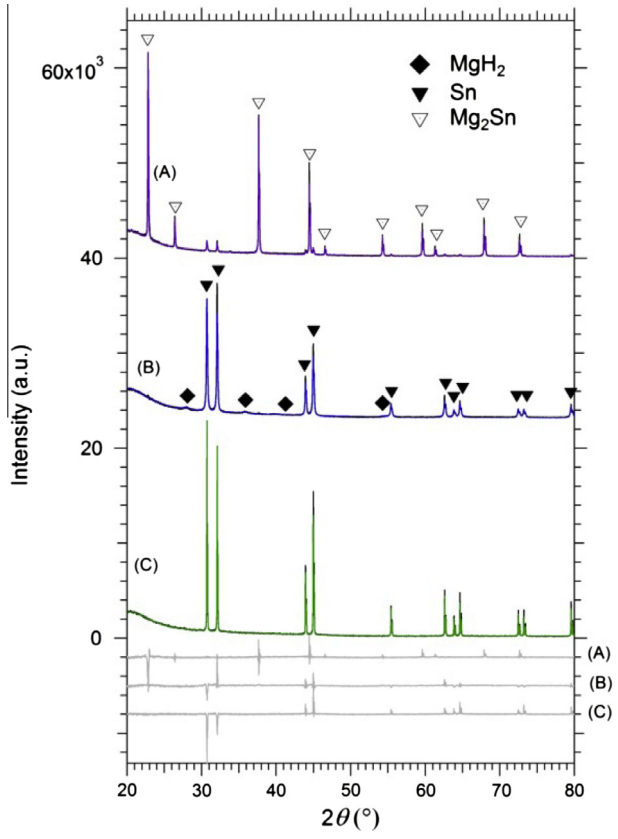

Fig. 4. XRD patterns of Sn based experiments (A) MgH_2 and Sn desorbed to form Mg_2Sn, 24 h in 50–350 °C increments (B) Cryomilled with MgH_2 for 30 min (C) Sn as supplied from Sigma–Aldrich.

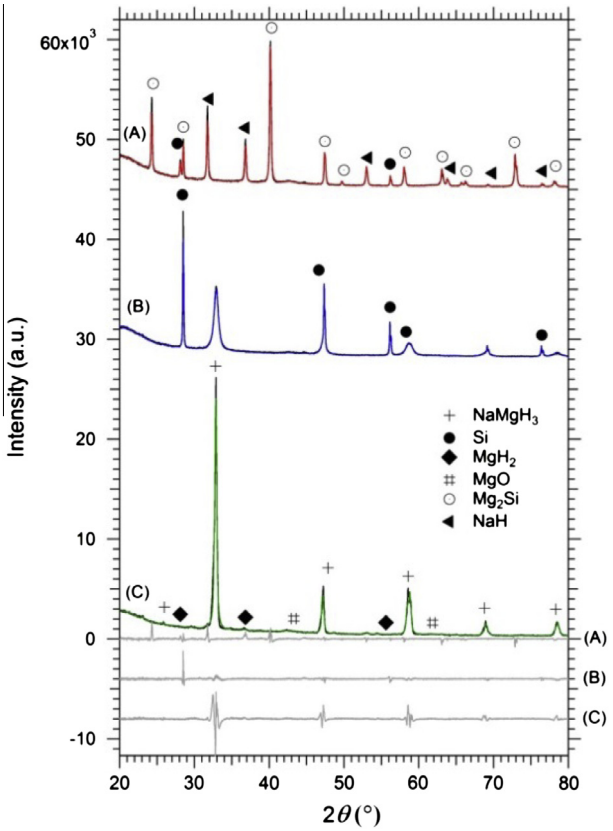

Fig. 5. XRD patterns of $NaMgH_3$ based experiments (A) $NaMgH_3$ and Si desorbed to form Mg_2Si and NaH, 24 h in 50–350 °C increments (B) Cryomilled with Si for 30 min (C) $NaMgH_3$synthesised from MgH_2 and NaH.

Prior to all desorption experiments, the materials as supplied by the manufacturer were characterised in terms of phases present and crystallite size (Table 1). XRD and Rietveld refinement results show that the MgH_2 contained approximately 3.7 wt.% Mg which would result in a lower than expected hydrogen capacity. The raw Si had no detectable contaminants. Ge had a small percentage of contamination, GeO_2, about 2.6 wt.%. However, there was little evidence of this phase in subsequent analysis as Mg/MgH_2 should reduce GeO_2 to form Ge and MgO. Sn, like Si, had no detectable contamination and had a different crystallite structure to both Si and Ge with a much larger crystallite size of 547 ± 16 nm. The synthesized $NaMgH_3$ had a similar level of minor oxidation as Sheppard et al. [20] with some MgO forming during the synthesis process.

After cryomilling each of the reactants in the correct stoichiometric ratios (Reactions (2)–(6), XRD was used to calculate the resulting crystallite sizes of each alloy present. From an initial crystallite size of 85 ± 1 nm, the size of β-MgH_2 was greatly reduced after cryomilling with Si, Ge and Sn producing sizes of 7.6 ± 0.1 nm, 5.6 ± 0.2 nm and 7.0 ± 0.6 nm respectively and pure β-MgH_2 cryomilled under the same conditions results in a crystallite size of 6.3 ± 0.1 nm. Each of the Group IV elements also reduced in crystallite size, but not to the same extent as MgH_2. It is common for a portion of pure MgH_2 to form metastable orthorhombic γ-MgH_2 during milling.[37] It was interesting to observe that cryomilling MgH_2 with Si (6.5 MohsScale) led to the formation of γ-MgH_2, however, this polymorph was not evident when milling with either Ge or Sn. One explanation is perhaps the presence of Ge (6 Mohs Scale) and Sn (4 Mohs) relieve the impact pressure

on MgH_2 thus preventing the formation of γ-MgH_2. Cryomilling $NaMgH_3$ with Si mixed the reagents and reduced the crystallite size as expected without effecting the structure of either $NaMgH_3$ or Si.

In order to gauge homogeneity of mixing and morphological information of the cryomilled powders, each milled sample containing MgH_2 and Group IV elements was analysed with SEM. Backscattered electron (BSE) images of these samples are shown in Fig. 6a, c and e. The BSE images highlight elements of heavier atomic mass as brighter regions. All samples were viewed under similar conditions (magnification, spot size, electron voltage and working distance) to easily compare differences or similarities. The milled MgH_2/Si sample (Fig. 6a) shows that the reagents are well mixed. Analysis is made difficult because there is little difference in contrast MgH_2 and Si as they have similar atomic mass.

However, the slightly brighter regions can be attributed to Si particles. Si particles appear to be slightly larger in size to MgH_2, which is expected due to the hardness of Si and consequently the difficulty in particle size refinement during milling. With the higher atomic masses of Ge and Sn, the contrast between MgH_2 and Ge (Fig. 6c) and Sn (Fig. 6e) is more apparent. The micrographs show that each of the reactants is well dispersed after mixing with the cryomill. Similar to Si, Ge and Sn particle sizes are larger than MgH_2. All the micrographs of the cryomilled materials show a large spread in particle size distribution ranging from 100 nm through to a few microns.

This result is similar to previous research into ball milled MgH_2 and Ge, where the authors found a large particle size distribution ranging from 10 μm particles to the sub-micron range [29].

The hydrogen desorption behaviour of as-milled samples was observed using a manometric Sieverts apparatus (Fig. 7) and temperature programmed desorption (TPD) instrument (Fig. 8). All of the mixtures showed little or no hydrogen desorption at the lower temperatures of 50 °C and 100 °C.

As indicated in Fig. 7a desorption of Si/MgH_2 began at 250 °C and, as expected, an increase in temperature lead to an increase in reaction kinetics although the sample was not fully desorbed until 350 °C. These results are in agreement with Paskevicius et al. [22] where MgH_2 ball milled with Si for 24 h desorbed in the range of 250 °C and 350 °C. XRD post reaction resulted in the presence of Mg_2Si with near complete conversion, 97 wt.% (Fig. 2a). Again the theoretical hydrogen content of 5 wt.% was not reached due to the impurity of Mg detected in the MgH_2. Sieverts apparatus desorption obtained a final H_2 release of 4.81 wt.%, 96% of the theoretical value. BSE SEM on the sample after Sieverts apparatus desorption (Fig. 6b) correlates with near full conversion to Mg_2Si, showing a homogenous mixture in terms of atomic weight (no contrast variation) as well as particle size

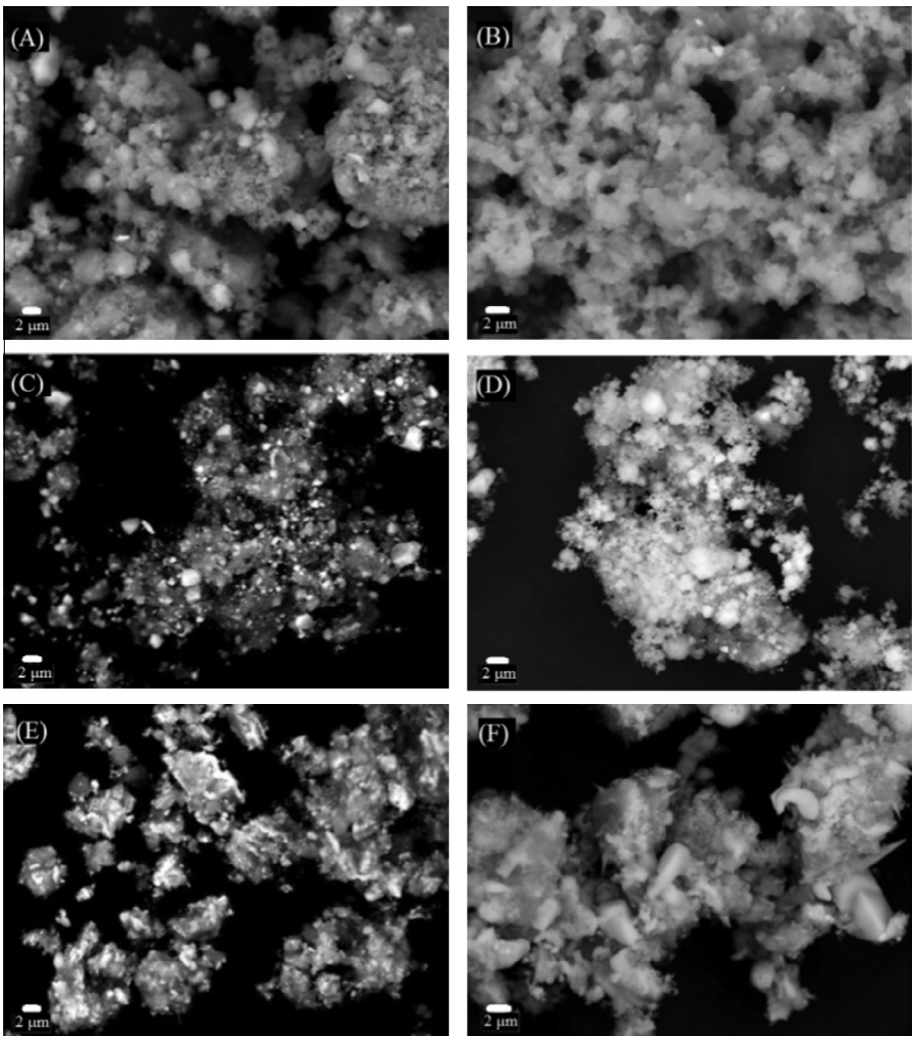

Fig. 6. SEM BSE images (accelerating voltage 20 kV) of (A) $2MgH_2$ + Si (B) Mg_2Si (C) $2MgH_2$ + Ge (D) Mg_2Ge (E) $2MgH_2$ + Sn (F) Mg_2Sn.

(average size less than 1 μm). The desorption temperature during TPD measurements was also higher for the Si mixture than either Ge or Sn, where desorption occurred as a single event at a temperature of 350 °C. This value was marginally lower than MgH_2 cryomilled under the same conditions (desorption temperature of 370 °C), again restating the fact that this reaction is kinetically limited despite the thermodynamic destabilisation effect of Si addition. The single decomposition peak indicates that Mg diffusion into the Si matrix occurs in one kinetically limited step, implying that the particle size distribution was narrower. Another study that involved TPD also gave single peak desorption, however at a lower temperature (290 °C), as a different heating rate was used and the sample was under a helium atmosphere, not under vacuum [23]. An important point to note for the Group IV element samples added to MgH_2 was that all desorption temperatures were lower than pure MgH_2 (365 °C).

MgH_2 with Ge was the first mixture to begin hydrogen release at 150 °C; although this step was kinetically slow, as indicated by the shallow incline at 150 °C in Fig. 7b. The majority of hydrogen desorbed from this mixture at higher temperatures (200–250 °C) with faster reaction rates (steeper inclines Fig. 7b) until it completely desorbed at 300 °C. XRD from the decomposed sample is given in Fig. 3a and reveals almost complete conversion to Mg_2Ge. No evidence of MgH_2 peaks could be detected using XRD, however, traces of Ge still remained. The total quantity of hydrogen released from the Sieverts desorption was 2.91 wt.% H_2, slightly lower than the theoretical value of 3.22 wt.%. The marginally lower experimental value is attributed to both Ge and MgH_2 containing small amounts of Mg and GeO_2, as indicated by the XRD prior to desorption (Figs. 2b and 3b). MgH_2 has a purity of ~95% therefore all desorption reactions would not reach theoretical desorption values due to the presence of impurities. The BSE image from SEM (Fig. 6d) after desorption also shows a more homogeneous morphology of smaller particles when compared to the pre-desorption image. Also, there is no significant brightness contrast indicating that an almost full conversion to a single phase has taken place as differences in the atomic mass are not observed.

Temperature programmed desorption from the MgH_2 and Ge mixture also began at a lower temperature (260 °C) compared to all other materials (Fig. 8c). It was unexpected that this TPD would contain two decomposition events. This indicates that the decomposition is two-step, either due to an intermediate decomposition product, or a two-stage kinetic process. To understand this phenomenon, a second TPD was performed and halted at 300 °C (after the first peak was fully resolved) and the sample cell quenched in liquid nitrogen to prevent any further reaction. The resultant XRD is shown in Fig. 9a. There are no unknown structures other than the expected MgH_2, Ge and Mg_2Ge. That is, there are no unexpected intermetallics present, such as MgGe. The second desorption peak can be explained by the wide range in particle size that

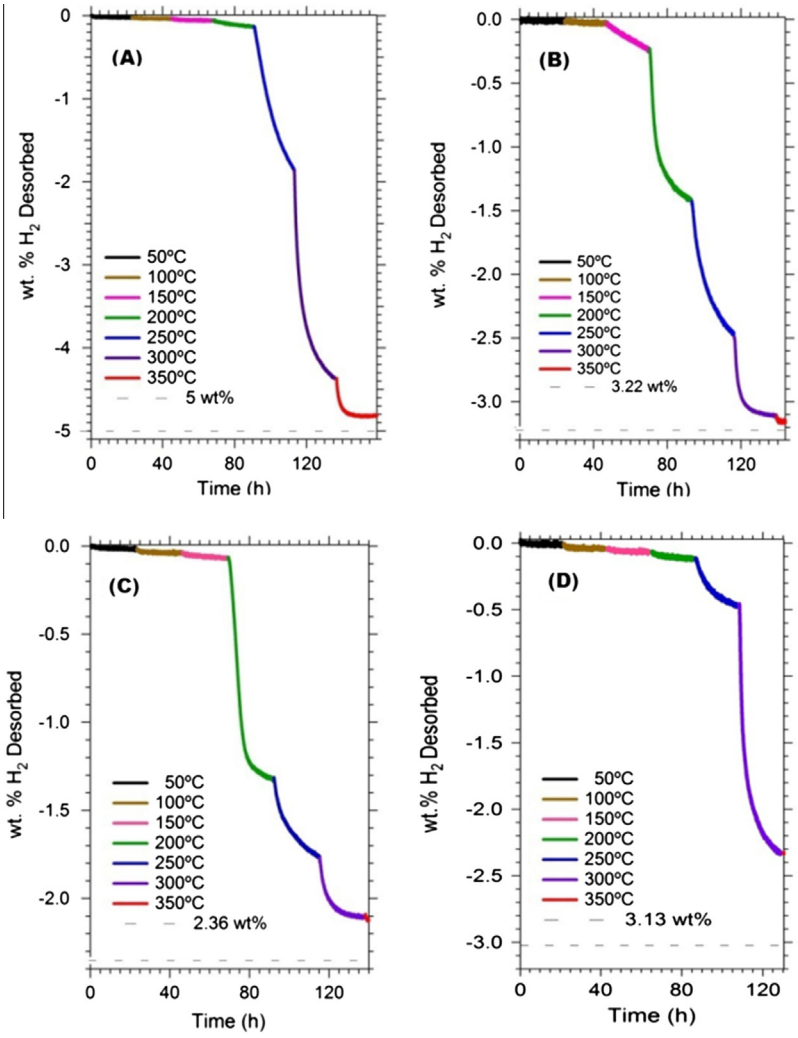

Fig. 7. Time and temperature relationship with wt.% of H_2 desorbed from (A) $2MgH_2$ + Si (B) $2MgH_2$ + Ge (C) $2MgH_2$ + Sn (D) $2NaMgH_3$ + Si.

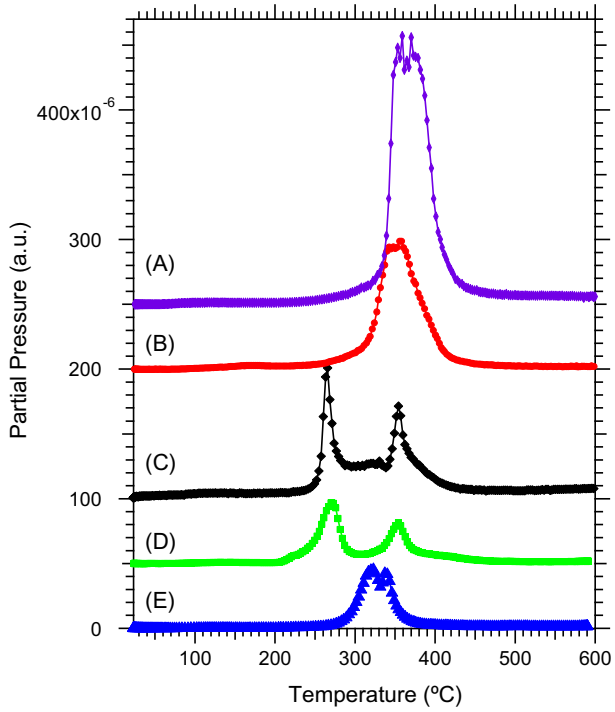

Fig. 8. Mass spectra of desorbed gases from: (A) Pure MgH_2 (B) $2MgH_2$ + Si (C) $2MgH_2$ + G0065 (D) $2MgH_2$ + Sn (E) $2NaMgH_3$ + Si.

causes two-step kinetic behaviour. The particle size distributions must be significantly different enough such that diffusion of Mg and Ge occurs in two stages, one temperature (260 °C) for the smaller particle range, approximately 100 nm or below, and a higher temperature of 350 °C for the larger (micron sized) particles. This is in contradiction to Walker et al. [29] who attributed a single peak in DSC measurements to be the thermodynamic event of MgH_2 dehydrogenation despite a large variation in particle size.

Sn with MgH_2 began desorption at 200 °C as detected using the Sieverts apparatus. However, full desorption did not occur after 24 h at this temperature. Once the temperature increased to 250 °C and then 300 °C, the rate of reaction slowed and by 350 °C the sample was fully desorbed. Fig. 4a shows the resultant XRD after desorption with an almost full conversion to 94 wt.% Mg_2Sn. Again the Sieverts measurements gave a slightly lower hydrogen release of 2.15 wt.% H_2 when compared to the theoretical storage capacity of 2.36 wt.%. SEM results give an interesting change in morphology of the reacted Mg_2Sn that was not seen in any other sample (Fig. 6f). Although largely homogenous in atomic mass (no contrast differences), well defined obelisk shaped particles of various sizes were detected, typically quite large, ~5 μm. This is possibly due to the fact that the melting point of Sn is only about 232 °C. The XRD after halting the TPD at 300 °C (Fig. 9b) showed that some Sn remained so this could have melted and agglomerated. This is in contrast to the MgH_2/Sn morphology in the as-synthesised ball milled sample, which is more spherical in structure [38]. Similar to the reaction containing Ge, Sn with MgH_2 also resulted in two-step decomposition during the TPD experiment likely due to the wide particle size distribution. The initial hydrogen release peak occurred at 270 °C with the second at 360 °C as shown in Fig. 8d. A double desorption peak was also displayed during a TPD experiment [31] with balled milled MgH_2 and Sn with the addition of cyclohexane. This different preparation technique of ball milling with cyclohexane reduced the temperature of the peaks to 217 °C and 257 °C [31]. The authors of this study [31] concluded that the formation of the two desorption events was due to the existence of two types of hydrogen species in the Sn/MgH_2 composite, however, our XRD results contradict this statement. Similar to the Ge system, the TPD was repeated and stopped at 300 °C and the XRD (Fig. 9b) showed no unexpected intermediate phases. Therefore, the two-step decomposition can be most likely attributed to the variation in particle size, resulting in different diffusion rates for Mg and Sn to form Mg_2Sn. Both of the Ge and Sn samples mixed with MgH_2 appeared to have less kinetic limitations than Si with MgH_2.

Sieverts desorption results for the $NaMgH_3$/Si system are shown in Fig. 7d. Initially, desorption occurred at a consistently slow rate until 250 °C, where the rate increased. The majority of desorption however, occurred at 300 °C, 80 °C lower than pure $NaMgH_3$ at 1 bar of pressure_ENREF_3. Similar, to the previous mixtures, a lower experimental value was reached for the total quantity of hydrogen desorbed, 2.34 wt.%, compared to the theoretical value of 3.13 wt.%. TPD results (Fig. 8e) show overlapping peaks occurring at maximum temperatures of 320 °C and 340 °C. As with Ge and Sn addition to MgH_2, this could be the result of differing particle sizes.

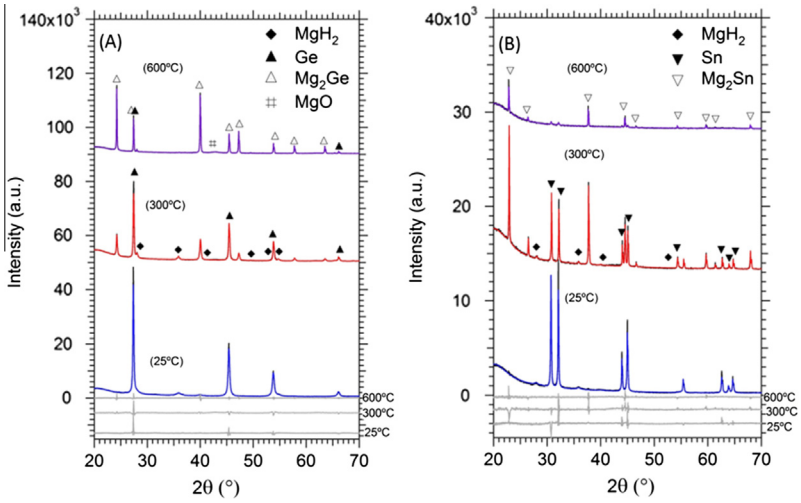

Fig. 9. XRD taken after heating to before (25 °C), during (300 °C) and after (600 °C) RGA analysis (A) $2MgH_2$ + Ge (B) $2MgH_2$ + Sn.

4. Conclusions

A direct comparison of the addition of Si, Ge and Sn showed interesting results when each mixture was prepared under identical conditions. Each of the Group IV elements added to MgH_2 and Si to $NaMgH_3$, successfully lowered the decomposition temperature, however, it appears reaction kinetics play a larger role than thermodynamics in the decomposition reaction. It appears that the system that contained Ge and MgH_2 had the fastest reaction kinetics since it started desorption at the lowest temperature of 150 °C, although it undertook two-step decomposition. Sn also had a significant effect on MgH_2 with desorption occurring at 200 °C. Si, with comparison to the other Group IV elements, had a lesser effect on MgH_2 with desorption initiated at 250 °C. This study also provided information on the influence of Si on the $NaMgH_3$ compound. Reduction in desorption temperatures for all materials was observed, however kinetic limitations ensured that thermodynamic equilibrium conditions were not achieved. This indicates that kinetics have a significant role in each of the systems studied. Since differences in particle size were considered significant, the differences in kinetics are most likely due to different orders of reaction for nucleation and possibly growth due to particle size.

Acknowledgements

AC acknowledges Curtin University for granting the Postgraduate Scholarship and Research Scholarship (CUPS and CURS) as well as the Australian Commonwealth Scientific and Research Organisation (CSIRO) for providing funding for the project. AC also acknowledges Elaine Miller for her assistance with the SEM at Curtin University. CEB, MP and DAS acknowledge the financial support of the Australian Research Council for ARC Linkage Grant LP120100435, and CEB acknowledges the ARC for ARC LIEF Grants LE0775551 and LE0989180.

References

[1] D.M. Abrams, R.J. Wiener, A model of peak production in oil fields, Am. J. Phys. 78 (2010) 24–27.
[2] D.J. Arent, A. Wise, R. Gelman, The status and prospects of renewable energy for combating global warming, Energy Econ. 33 (2011) 584–593.
[3] N.A. Kelly, T.L. Gibson, M. Cai, J.A. Spearot, D.B. Ouwerkerk, Development of a renewable hydrogen economy: optimization of existing technologies, Int. J. Hydrogen Energy 35 (2010) 892–899.
[4] J. Brouwer, On the role of fuel cells and hydrogen in a more sustainable and renewable energy future, Curr. Appl. Phys. 10 (2010) S9–S17.
[5] P.P. Edwards, V.L. Kuznetsov, W.I.F. David, N.P. Brandon, Hydrogen and fuel cells: towards a sustainable energy future, Energy Policy 36 (2008) 4356–4362.
[6] M. Hirscher, Handbook of Hydrogen Storage: New Materials for Future Energy Storage, 2009.
[7] U. Department of Energy, Targets for OnBoard Hydrogen Storage Systems for Light-Duty Vehicles, Office of Energy Efficiency and Renewable Energy and The FreedomCAR and Fuel Partnership, 2009.
[8] U. Bösenberg, C. Pistidda, M. Tolkiehn, N. Busch, I. Saldan, K. Suarez-Alcantara, A. Arendarska, T. Klassen, M. Dornheim, Characterization of metal hydrides by in-situ XRD, Int. J. Hydrogen Energy 39 (2014) 9899–9903.
[9] L.H. Jepsen, M.B. Ley, Y.-S. Lee, Y.W. Cho, M. Dornheim, J.O. Jensen, Y. Filinchuk, J.E. Jørgensen, F. Besenbacher, T.R. Jensen, Boron–nitrogen based hydrides and reactive composites for hydrogen storage, Mater. Today 17 (2014) 129–135.
[10] M.B. Ley, L.H. Jepsen, Y.-S. Lee, Y.W. Cho, J.M. Bellosta von Colbe, M. Dornheim, M. Rokni, J.O. Jensen, M. Sloth, Y. Filinchuk, J.E. Jørgensen, F. Besenbacher, T.R. Jensen, Complex hydrides for hydrogen storage – new perspectives, Mater. Today 17 (2014) 122–128.
[11] D.A. Sheppard, M. Paskevicius, C.E. Buckley, The mechanochemical synthesis of magnesium hydride nanoparticles, J. Alloys Comp. 492 (2010) L72–L74.
[12] A.Y. Yermakov, N.V. Mushnikov, M.A. Uimin, V.S. Gaviko, A.P. Tankeev, A.V. Skripov, A.V. Soloninin, A.L. Buzlukov, Hydrogen reaction kinetics of Mg-based alloys synthesized by mechanical milling, J. Alloys Comp. 425 (2006) 367–372.
[13] R. Schulz, J. Huot, G. Liang, S. Boily, G. Lalande, M.C. Denis, J.P. Dodelet, Recent developments in the applications of nanocrystalline materials to hydrogen technologies, Mater. Sci. Eng. A – Struct. 267 (1999) 240–245.
[14] J. Huot, G. Liang, R. Schulz, Mechanically alloyed metal hydride systems, Appl. Phys. A – Mater. 72 (2001) 187–195.
[15] M.P. Pitt, M. Paskevicius, C.J. Webb, D.A. Sheppard, C.E. Buckley, E.M. Gray, The synthesis of nanoscopic Ti based alloys and their effects on the MgH_2 system compared with the $MgH_2 + 0.01Nb_2O_5$ benchmark, Int. J. Hydrogen Energy 37 (2012) 4227–4237.
[16] M. Paskevicius, D.A. Sheppard, C.E. Buckley, Thermodynamic changes in mechanochemically synthesized magnesium hydride nanoparticles, J. Am. Chem. Soc. 132 (2010) 5077–5083.
[17] K. Ikeda, S. Kato, Y. Shinzato, N. Okuda, Y. Nakamori, A. Kitano, H. Yukawa, M. Morinaga, S. Orimo, Thermodynamical stability and electronic structure of a perovskite-type hydride, $NaMgH_3$, J. Alloys Comp. 446–447 (2007) 162–165.
[18] D. Pottmaier, E.R. Pinatel, J.G. Vitillo, S. Garroni, M. Orlova, M.D. Baró, G.B.M. Vaughan, M. Fichtner, W. Lohstroh, M. Baricco, Structure and thermodynamic properties of the $NaMgH_3$ perovskite: a comprehensive study, Chem. Mater. 23 (2011) 2317–2326.
[19] H. Wu, W. Zhou, T.J. Udovic, J.J. Rush, T. Yildirim, Crystal chemistry of perovskite-type hydride $NaMgH_3$: implications for hydrogen storage, Chem. Mater. 20 (2008) 2335–2342.
[20] D. Sheppard, M. Paskevicius, C. Buckley, Thermodynamics of hydrogen desorption from $NaMgH_3$ and its application as a solar heat storage medium, Chem. Mater. 23 (2011) 4298–4300.
[21] A.-L. Chaudhary, D.A. Sheppard, M. Paskevicius, M. Saunders, C. Buckley, Mechanochemical synthesis of amorphous silicon nanoparticles, RSC Adv. 42 (2014) 21979–21983.
[22] M. Paskevicius, D.A. Sheppard, A.L. Chaudhary, C.J. Webb, E.M.A. Gray, H.Y. Tian, V.K. Peterson, C.E. Buckley, Kinetic limitations in the Mg–Si–H system, Int. J. Hydrogen Energy 36 (2011) 10779–10786.
[23] M. Polanski, J. Bystrzycki, The influence of different additives on the solid-state reaction of magnesium hydride (MgH_2) with Si, Int. J. Hydrogen Energy 34 (2009) 7692–7699.
[24] J.J. Vajo, F. Mertens, C.C. Ahn, R.C. Bowman, B. Fultz, Altering hydrogen storage properties by hydride destabilization through alloy formation: LiH and MgH_2 destabilized with Si, J. Phys. Chem. B 108 (2004) 13977–13983.
[25] A.-L. Chaudhary, D.A. Sheppard, M. Paskevicius, C.J. Webb, E.M. Gray, C.E. Buckley, Mg_2Si nanoparticle synthesis for high pressure hydrogenation, J. Phys. Chem. C 118 (2014) 1240–1247.
[26] N.O. Folland, F. Bassani, Selection rules and Mg_2Si, Mg_2Ge and Mg_2Sn, J. Phys. Chem. Solids 29 (1968) 281–290.
[27] J.J. Martin, Thermal conductivity of Mg_2Si, Mg_2Ge and Mg_2Sn, J. Phys. Chem. Solids 33 (1972) 1139–1148.
[28] D. Zhou, J. Liu, S. Xu, P. Peng, Thermal stability and elastic properties of Mg_2X (X = Si, Ge, Sn, Pb) phases from first-principle calculations, Compd. Mater. Sci. 51 (2012) 409–414.
[29] G. Walker, M. Abbas, D. Grant, C. Udeh, Destabilisation of magnesium hydride by germanium as a new potential multicomponent hydrogen storage system, Chem. Commun. 47 (2011) 8001–8003.
[30] H. Imamura, K. Tanaka, I. Kitazawa, T. Sumi, Y. Sakata, N. Nakayama, S. Ooshima, Hydrogen storage properties of nanocrystalline MgH_2 and MgH_2/Sn nanocomposite synthesized by ball milling, J. Alloys Comp. 484 (2009) 939–942.
[31] H. Imamura, K. Yoshihara, M. Yoo, I. Kitazawa, Y. Sakata, S. Ooshima, Dehydriding of nanocomposite formed by ball milling of with Sn, Int. J. Hydrogen Energy 32 (2007) 4191–4194.
[32] H.C. Zhong, H. Wang, L.Z. Ouyang, M. Zhu, Microstructure and hydrogen storage properties of Mg–Sn nanocomposite by mechanical milling, J. Alloys Comp. 509 (2011) 4268–4272.
[33] B. Bogdanović, K. Bohmhammel, B. Christ, A. Reiser, K. Schlichte, R. Vehlen, U. Wolf, Thermodynamic investigation of the magnesium–hydrogen system, J. Alloys Comp. 282 (1999) 84–92.
[34] B.H. Toby, R factors in Rietveld analysis: how good is good enough?, Powder Diffr 21 (2006) 67–70.
[35] L. Topor, A. Navrotsky, Y. Zhao, D.J. Weidner, Thermochemistry of fluoride perovskites: heat capacity, enthalpy of formation, and phase transition of $NaMgF_3$, J. Solid State Chem. 132 (1997) 131–138.
[36] Y. Bouhadda, Y. Boudouma, N.-E. Fenineche, A. Bentabet, Ab initio calculations study of the electronic, optical and thermodynamic properties of $NaMgH_3$, for hydrogen storage, J. Phys. Chem. Solids 71 (2010) 1264–1268.
[37] J. Huot, G. Liang, S. Boily, A. Van Neste, R. Schulz, Structural study and hydrogen sorption kinetics of ball-milled magnesium hydride, J. Alloys Comp. 293–295 (1999) 495–500.
[38] T. Aizawa, R. Song, Mechanically induced reaction for solid-state synthesis of Mg_2Si and Mg_2Sn, Intermetallics 14 (2006) 382–391.